

Tribocorrosion Behavior of Overlay Welded Super Duplex Stainless Steel in Chloride Medium

Abbas Eghlimi¹  · Keyvan Raeissi¹ · Morteza Shamanian¹

Received: 25 March 2015 / Revised: 27 April 2015 / Accepted: 20 May 2015 / Published online: 2 June 2015
© Springer International Publishing AG 2015

Abstract The tribocorrosion behavior of super duplex stainless steel overlay weldment, sliding against alumina counterpart in a pin-on-disk tribometer in 1 M NaCl solution, was investigated under open circuit potential and potentiostatic conditions. The results demonstrated the significant effect of applied potential on the tribocorrosion behavior; by shifting the potentiostatic potential from cathodic to anodic range, the material degradation increased due to the introduction of synergistic wear-accelerated corrosion. Moreover, by shifting from cathodic to anodic potentiostatic polarization, the wear track became smoother and the coefficient of friction decreased. Although some evidences of corrosion-accelerated wear, such as occasional corrosion pits as well as reduction of work hardening inside the wear track, were observed, based on the synergistic approach followed, it was inferred that the dominant degradation components of the overlay welded specimen were sequentially wear and wear-accelerated corrosion.

Keywords Super duplex stainless steel · Overlay welding · Tribocorrosion · Wear-accelerated corrosion · Corrosion-accelerated wear · Wear topography

1 Introduction

Tribocorrosion refers to the transformation or degradation of material due to simultaneous action and interaction of mechanical wear and chemical/electrochemical processes

on the surface [1]. Coupling of mechanical and environmental effects during tribocorrosion action often causes the synergism or antagonism, i.e., negative synergy. As a result, the material loss due to tribocorrosion often considerably exceeds the simple sum of losses caused by mechanical wear and corrosion individually. This excess degradation occurs through cumulative and irreversible microscopic changes in the structure of the metal which not only occur in the wear track but also on the adjacent regions [2, 3].

Since tribocorrosion is a surface phenomenon, researchers usually aim at addressing the need to select and design new surfaces and to extend the life of available devices through application of resistant coatings [3–5]. One of the standard methods to enhance the corrosion resistance of engineering materials at an affordable price is corrosion-resistant alloy overlay welding. In this process, a thick layer of a corrosion-resistant alloy metal with a strong metallurgical bonding with the substrate is deposited through a welding process [6, 7]. However, because of their low surface hardness, corrosion-resistant alloys do not generally resist tribocorrosion well [1, 8]. Hence, considerable effort is now being made to research and enhance the performance of these coatings under tribocorrosion and to develop new superior alloys. Of the most promising alloys in this quest are duplex stainless steels (DSSs) and far superior highly alloyed super duplex stainless steels (SDSSs) which possess both good mechanical properties and corrosion resistance behavior.

Historically, DSSs were first developed in the 1930s to be used in pulp industry. But soon they have found many applications in paper, chemical, fertilizer, nuclear, food processing, and petrochemical industries where high strength and localized corrosion resistance, especially in chloride environments, are required [9, 10]. These alloys

✉ Abbas Eghlimi
a.eghlimi@ma.iut.ac.ir;
<https://aeghlimi.materials.iut.ac.ir>

¹ Department of Materials Engineering, Isfahan University of Technology, 84156-83111 Isfahan, Iran

are commonly used in applications dealing with sliding or friction in a corrosive media such as centrifugal separators [11], offshore and marine transportation of slurries [2], plumbing and pump components, and other particle-laden fluids. In these applications which mainly deal with erosion-corrosion, overlay welding of SDSSs on less noble substrates, such as carbon or high-strength low-alloy (HSLA) steels, proved to be a cost-effective method for producing protective coatings. However, in some cases, as in the case of pump components and also in direct-acting riser tensioner piston rods which are partly submerged into the sea and are operating in the splash zone, the movements of parts in the presence of lubricants can lead to catastrophic acceleration of coating degradation via extensive material loss through tribocorrosion [12]. These failures have also led to failure of SDSS coatings in the discharge section of centrifugal separators in marine industries where pressurized saline fluids act as the main lubricant.

It is well-known that the superior corrosion resistance of SDSSs, like other passive metals, is due to the formation of a dense high-resistant nanometric surface passive oxide film which is formed by reaction of the metal with the corrosive medium. When this film has reached a certain thickness, it acts like a diffusion barrier and suppresses the charge transfer through separation of the metal surface from the corrosive environment.

Generally, the magnitude of surface degradation during tribocorrosion depends on several factors, including (1) the material properties comprising chemical composition, surface hardness, density, microstructure, etc., (2) environmental factors containing pH, dissolved oxygen content, temperature, etc., (3) stability and performance of the passive film consisting of its adhesion, cohesion, depassivation and repassivation rate, etc., and (4) composition and thickness of the tribofilm, i.e., the nanometer-thick mechanically mixed layer which is formed in the shear zone between the contacting surfaces, which in turn depend on the coefficient of friction (COF) and mass transport [1, 13].

Although over the last years many authors have investigated the corrosion resistance of DSSs in different media, their tribocorrosion behavior was the subject of fewer studies [2, 14–19]. However, investigations on the structural changes during tribocorrosion test of other stainless steels [20, 21] showed that the total tribocorrosion degradation is mainly due to a phenomenon called depassivation. Depassivation normally occurs when rubbing causes a local damage or even removal of the passive film and leads to an accelerated anodic dissolution of the bare metal through charge transfer in the galvanic cell formed between the worn and unworn surfaces. The additional damage caused by depassivation is usually called wear-accelerated/induced corrosion loss.

However, wear-accelerated corrosion is not the only synergistic term involved in tribocorrosion, because the

presence of oxide films or corrosion products on the surface asperities can also alter the level of frictional work and the resulting surface temperatures. This type of synergy is usually called corrosion-accelerated/induced wear. In the case of DSSs, the presence of harder carbide/nitride or intermetallic precipitates, such as χ and σ , on the surface establishes a micro-corrosion cell owing to their different chemical compositions and thus, different corrosion resistances. This situation can result in the preferential anodic dissolution of the area close to or at the matrix/precipitates interface [22–24] and thereby can accelerate the precipitates removal from surfaces and intensify the material loss.

The current study seeks to evaluate the sliding tribocorrosion mechanisms of overlay welded SDSS on HSLA steel substrate, produced using constant current gas tungsten arc welding, in 1 M NaCl solution. The results of this work can be used to predict the service life and failure mode of SDSS overlaid components and to prevent their tribocorrosion degradation.

2 Experimental Procedure

2.1 Materials and Overlay Welding Process

In the current study, a SDSS with the chemical compositions presented in Table 1 was deposited in two layers on HSLA steel substrates. The overlay welding process was carried out in the flat position with constant current parallel to the substrate rolling direction. Accordingly, a thick layer of the SDSS weld metal was deposited onto the HSLA steel base using cold wire gas tungsten arc welding process to obtain a corrosion-resistant top coating. The procedure consisted of the deposition of several weld beads arranged side by side which led to the formation of a continuous surface layer. The welding parameters were chosen based on previous studies [25, 26] and are summarized in Table 2.

2.2 Microstructure Examinations

After the overlay welding process and proper post cleaning, the metallographic specimens were cut from the cross section and top surface, ground mechanically, polished with 0.3 μm alumina powder, and electro-polished in a solution consisting 25 g CrO_3 , 133 mL acetic acid, and 7 mL distilled water. Then, nital 2 % was used to etch the substrate. SDSS sections were electro-etched in 40 % NaOH at 3–5 V direct current (DC). UNS S30403 austenite stainless steel was used as cathode in electro-polishing and electro-etching processes. The surface was examined by Philips XL 30 scanning electron microscope (SEM) and the

Table 1 Chemical composition of substrate and filler metal (wt. %)

Material	C	Cr	Ni	Mo	N	Mn	Si	Cu	PREN ^a
Filler metal	0.03	25.9	9.2	4.2	0.22	0.75	0.94	0.54	46.36
Substrate	0.26	0.02	–	0.05	–	1.36	0.41	0.05	–

^a Pitting Resistance Equivalent Number (PREN) = Cr + 3.3 Mo + 30 N (wt. %)

Table 2 Constant parameters used for overlay welding

Parameter	Value
Shielding gas	Pure (99.99 %) Argon
Shielding gas flow rate	10 L min ⁻¹
Filler rod diameter	2.4 mm
Welding electrode	2.4 mm ISO 6848 WTh 20 (98 % W + 2 % ThO ₂)
Polarity	Direct current electrode negative (DCEN)
Max inter-pass temperature	150 °C
Heat input	0.94 kJ mm ⁻¹

volume percent of the ferrite phase was obtained for 20 images at 200× magnification using the point counting method in accordance with ASTM E562.

2.3 Corrosion Tests

For corrosion experiments, small rectangular samples were cut from the top coating, ground mechanically down to 1200 grit SiC paper, rinsed under distilled water, and dried in hot air. Before putting the specimens into the electrochemical cell, the test area of 1 cm² was created by masking all other areas using lacquer. The corrosion resistance was evaluated by means of electrochemical measurements under natural aerated condition in 1 M NaCl solution at 25 °C. For these experiments, an electrochemical cell kit consisting of Ag/AgCl electrode (SSE) as reference electrode and an auxiliary platinum (Pt) electrode was used; the working electrode, i.e., the sample to be investigated, was fixed at the bottom of the electrochemical cell.

After stabilization of open circuit potential (OCP), i.e., the potential established when the cathodic and anodic reactions take place at the same rate, polarization curve was recorded dynamically at the scan rate of 1 mV s⁻¹ from -250 mV_{OCP} to a potential corresponding to 5 mA cm⁻² current density using an AMETEK PARStat[®] 2273 Potentiostat. Three measurements were performed to ensure reproducibility of results.

2.4 Tribocorrosion Measurements

Before tribocorrosion testing, the overlay welded specimens were embedded with a three-component resin-based insulating material, ground mechanically down to 1200 grit SiC paper, and then, polished using diamond paste to achieve a mirror-like surface with roughness value of <0.3 μm. Then, the samples were rinsed in distilled water,

and dried in hot air for using in tribocorrosion experiments. Before starting the tests, an exposed area of 2 × 2 cm² was prepared by masking all other areas except overlay welded surface using epoxy-based insulating material.

Experimentally, to simulate the tribocorrosion process in laboratory conditions, an inert counterpart is rubbed against the passive metal to measure the electrochemical and mechanical responses/parameters [1]. In the current study, the tribocorrosion properties of the material were evaluated using reciprocating sliding established by rubbing an alumina ball of 4.2-mm diameter against the samples immersed in 1 M NaCl solution. The tribocorrosion test system is illustrated in Fig. 1. This system was assembled by integrating a tribometer and an electrochemical potentiostat. In order to electrically isolate the specimen from the tribometer, the corrosion cell kit was made of polyamide nylon. Such a setup ensured that only the exposed test area of the specimen was subjected to corrosion attack during the test. EG&G[®] 263A Potentiostat was used to control the potential of the samples. The reference and auxiliary electrodes were SSE and Pt, respectively. All the tests were performed at room temperature (~25 °C) and open to air. During the test, the alumina ball, held in the test cell, was sliding against the working electrode, under controlled normal force of 19.6 N, sliding frequency of 1 Hz, and the stroke length of 10 mm. Such a load corresponded to an average Hertzian pressure of 745 MPa.

Tribocorrosion experiments were performed in a reciprocating motion apparatus under three electrochemical potentiostatic polarizations: cathodic potential (-500 mV_{SSE}), OCP, and anodic potential (+700 mV_{SSE}). The testing potentials were selected from the recorded polarization curves. To investigate the possibility of hydrogen charging of the test specimen, and thus, hydrogen embrittlement during sliding under cathodic potentials, one more test was

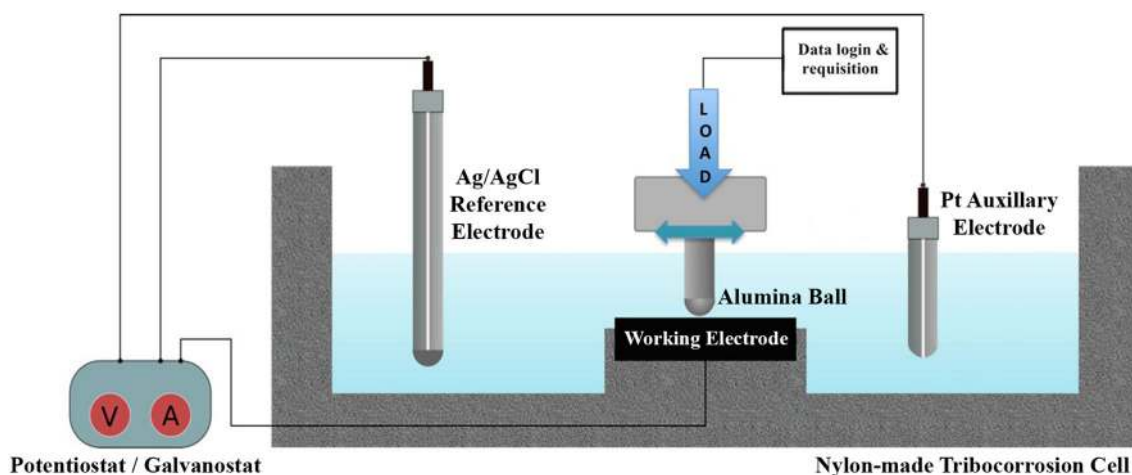


Fig. 1 Schematic representation of the tribocorrosion cell

performed at $-700 \text{ mV}_{\text{SSE}}$. The COF and current were measured continuously during the experiments. The experiments consisted of 5 steps: (1) cathodic cleaning of the samples at -1.2 V for 1 min, (2) stabilization of the OCP before applying potential, (3) application of the selected potential (either anodic or cathodic potentiostatic polarizations) for 10 min, (4) rubbing under applied potential for 30 min (1800 cycles), and (5) standby at the applied potential for 25 min after rubbing. To ensure reproducibility, the measurement was repeated three times with a new alumina ball and sample.

After tribocorrosion measurements, the volume loss was quantified by measuring the surface profiles across each wear track at three locations (one-fourth, one-half, and three-fourth of the stroke length) using a Mitutoyo SurfTest SJ-301 profilometer. The average cross-sectional area of the wear track was then estimated from the profiles by numerical integration, and the total wear volume was obtained by multiplying the average cross-sectional area by the length of the wear track which was roughly equal to the stroke length. The surface topography was examined by optical microscopy as well as SEM. Vickers microhardness ($\text{HV}_{0.1}$) measurement was also carried out on the surface of samples for all exposure conditions, both inside and outside the wear tracks. A digital Vickers microhardness tester (Micromet 5101) with an applied load of 100 gf for 15 s was used for these measurements. The indentation depths were between 2 and 3 μm , suggesting that the microhardness measurements were not influenced by the surface roughness and providing good hardness assessment of the affected surface.

During the pin-on-disk experiment, the surface of the counterpart alumina ball is always in contact with the specimen. Thus, analyzing the micrographs of the worn alumina balls is very helpful for precise determination of

the wear mechanism. Accordingly, after each test, the counterpart alumina ball was detached from its holder and its surface was studied with optical microscope. Then it was washed to remove all the corrosion and wear products and weighed. The volume loss of the alumina balls was calculated from changes in the weight measured before and after sliding using an electronic balance with a sensitivity of 10^{-5} g . In the plots discussed in the results section, each data point of the wear volume loss represents the average volume loss for the three alumina balls used in each test.

The specific wear rates (W_s) of both SDSS overlay weldments and alumina balls were calculated based on the Holm-Archard [27, 28] as the mass loss (Δm) or volume loss (ΔV) per distance ($L = 1800 \text{ cm}$) and applied load ($F_p = 19.6 \text{ N}$) using the following formula where ρ is the density ($\rho_{\text{ball}} = 3.95$ and $\rho_{\text{specimen}} = 7.8 \text{ g cm}^{-3}$):

$$W_s = \frac{\Delta m}{L\rho F_p} = \frac{\Delta V}{LF_p} \quad (1)$$

3 Results

3.1 Microstructure Evaluation

A full microstructure description of the top surface of SDSS overlay weldment can be found elsewhere [26, 29]. Here, the most remarkable microstructural features are outlined. As can be seen in Fig. 2a, the interface between the overlay weldment and substrate was planar, following by cellular and dendritic structures which suggest a sufficient metallurgical bond between the coating and the substrate. Moreover, based on Fig. 2b, although the top surface of the overlay weldment mainly consisted of grain boundary austenite (GBA) and Widmanstätten austenite

(WA), due to the multi-run process utilized, some intragranular austenite (IGA) and sporadic partially transformed austenite (PTA) morphologies were also observed. Regarding the total amount of austenite, it was on average around 62 volume percent.

3.2 Electrochemical Measurements

Figure 3a shows the potentiodynamic polarization curve of SDSS overlay weldment measured in 1 M NaCl solution. Four well-defined regions can be observed on this curve: (1) the cathodic domain with potentials below the corrosion potential (E_{corr}), (2) the cathodic–anodic transition region around E_{corr} , (3) the passive plateau extended from E_{corr} to the breakdown potential which, because ambient temperature is less than the critical pitting temperature for SDSSs, is in fact the transpassive dissolution critical potential (E_{tr}) [30], and (4) the transpassive dissolution region of the passive film beginning at E_{tr} . In the cathodic region, due to the reduction of hydrogen, the potential measured was negative. The current fluctuations in the passive region, from -200 to 0 mV_{SSE}, are associated with the metastable pitting events as a result of dissolution of chromium nitrides [31–33]. Generally, these metastable pitting activities in SDSSs can be observed at potentials below the critical pitting potential at which the metal salt of the chloride aggressive ion in solution is in equilibrium with the metal oxide and stable pitting growth starts.

Based on the results obtained, it is obvious that the overlay weldment showed a broad passive range with a high E_{tr} value. This is due to the slow cooling rate governed during the overlay welding which favored a good distribution of alloying elements between the austenite and ferrite which retarded the heterogeneous nucleation of IGA on Cr₂N particles [26]. However, at the onset of breaking down of the protective passive film, the current increased abruptly with the potential.

3.3 Tribocorrosion Tests

3.3.1 OCP Measurements

The measurement of OCP during sliding is a simple technique that can give valuable information about the surface state of the sliding metal. It is well-known that when a surface is tested at OCP during tribocorrosion testing, potential shifts cathodically to lower values [34]. This cathodic shift is due to the establishing of a galvanic cell between the active worn area inside the wear track and the passive worn or unworn areas inside or outside the wear track. Thus, as stated in the mixed potential theory [35], the OCP value recorded during sliding is a mixed potential which reflects the relative state between the active and passive areas. This mixed potential is mainly dependent on the surface area ratio of active (anodic) and passive (cathodic) areas, the repassivation kinetics of the passive film, and the anodic/cathodic polarization properties of the material [34].

The result of tribocorrosion testing under OCP condition is presented in Fig. 3b. Since the sample was in the passive state before starting the test, the OCP remained constant before application of the load. However, upon loading, a sudden negative shift took place. As discussed previously, this indicates that some parts of the material were moved to an active state. During loading, some slight oscillations in OCP occurred which could be associated to the galvanic coupling built up between the active and passive regions [36], formation of third bodies in the wear track, and competition between repassivation and depassivation [37]. If these oscillations are neglected, it can be seen that as rubbing continued, the potential decreased continually. This decrease was not due to an increase in the contact area or even change in the contact properties, because COF reduced with time during rubbing (see Fig. 3b). Rather, this

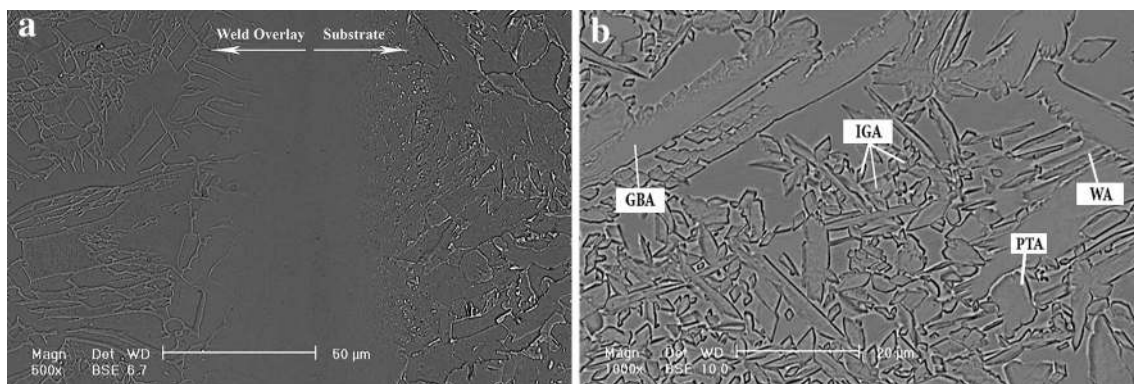
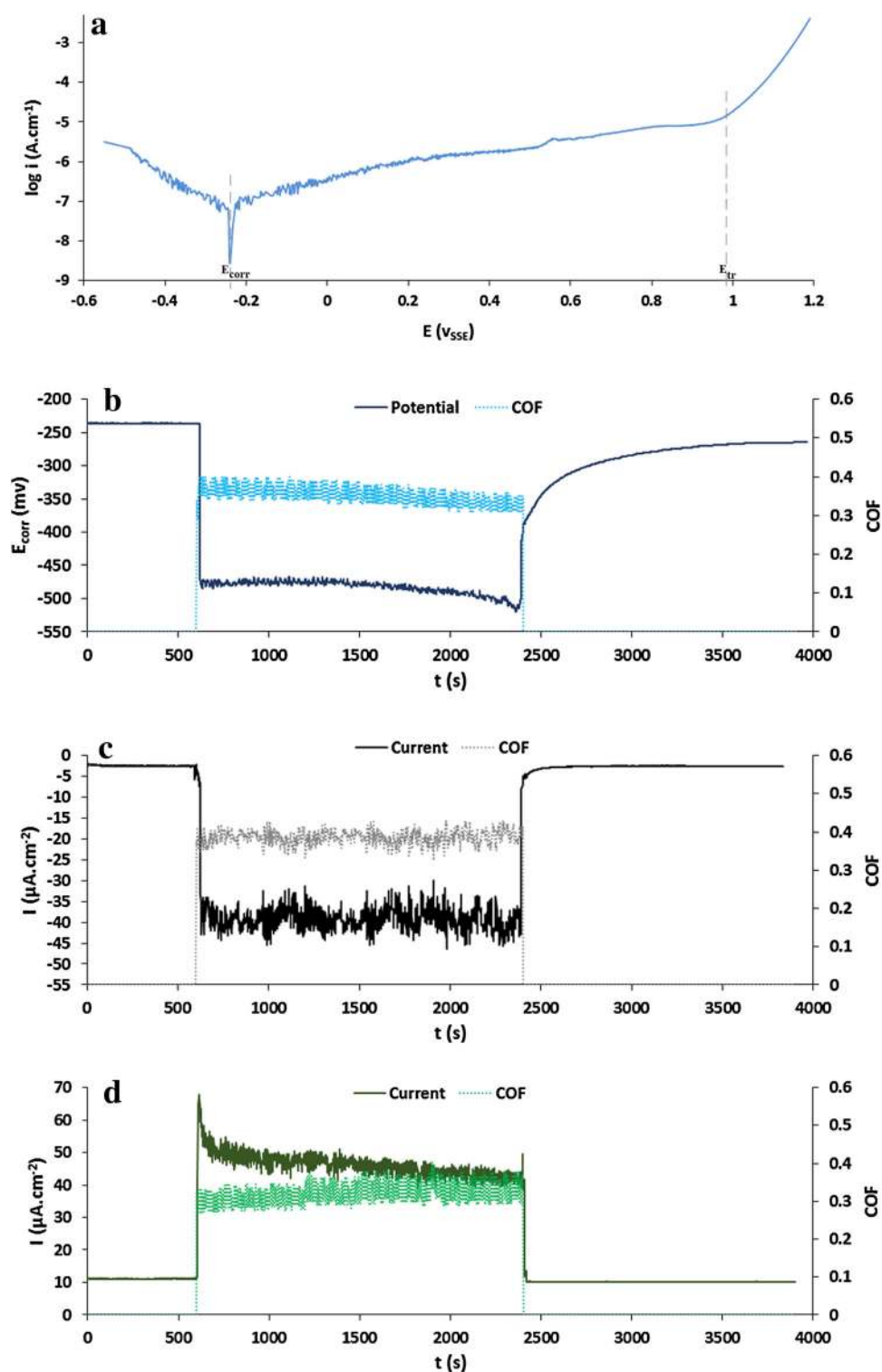


Fig. 2 a The cross section and b the top-surface microstructure of the overlay weldment

Fig. 3 **a** The polarization curve, **b–d** evaluation of potential, current, and COF during tribocorrosion testing in 1 M NaCl solution under **b** OCP, **c** cathodic potentiostatic polarization ($-500\text{ mV}_{\text{SSE}}$), and **d** anodic potentiostatic polarization ($+700\text{ mV}_{\text{SSE}}$)



may result from the increase in the active to passive surface ratio or dissolution of ejected wear debris [38]. Finally, due to the complete repassivation that occurred after unloading, the OCP increased and reached the initial values observed just before loading.

3.3.2 Cathodic Potentiostatic Measurements

During tribocorrosion at OCP, because no external current is exerted, the material and the electrolyte are at equilibrium and thus, the total net current is zero. This situation

impedes the proper evaluation of the corrosion kinetics and quantification of the contributing wear mechanisms. Thus, in order to quantify the contribution of different degrading mechanisms, tribocorrosion tests under cathodic and anodic potentiostatic conditions were conducted.

Cathodic potentiostatic tribocorrosion experiment was performed at a constant cathodic potential of $-500 \text{ mV}_{\text{SSE}}$ which was chosen based on Fig. 1. During testing at OCP, the cyclic mechanism of passive film abrasion and subsequent corrosion of the bare metal enhances the material wastage. However, under cathodic potentiostatic polarization, corrosion is negligible, and thus, the material degradation proceeds mainly through the mechanical wear [39, 40].

As can be seen in Fig. 3c, when rubbing started, the measured cathodic current density rapidly increased. This negative shift was due to the increase in cathodic reactions rate, which in turn was related to the formation of the rough track area as well as the hydrogen evolution, which were created and adhered to the metal surface, as a result of the interaction of the surface by the moving alumina ball [41]. Strain hardening of the surface exerted by mechanical wear may also have a role in increasing the cathodic reaction rate [1]. During rubbing, some current fluctuations can be seen at fairly regular time intervals which, based on the oscillation of COF during rubbing, could be attributed to the formation and ejection of wear debris [40]. When rubbing stopped, due to the complete recovery of worn track surface, the current had shifted toward the values observed prior to rubbing.

3.3.3 Anodic Potentiostatic Measurements

In this study, anodic potentiostatic tribocorrosion experiments were performed at the constant potential of $+700 \text{ mV}_{\text{SSE}}$. This potential was within the typical passive potential region (see Fig. 3a). Figure 3d shows the evolution of current and COF with time during anodic potentiostatic tribocorrosion test. During sliding, the protective oxide film of the SDSS on the contact areas is either removed or damaged after a single cycle or a certain number of sliding cycles and led to wear-accelerated corrosion. This depassivation was the main reason for the abrupt current increase by commencement of the rubbing. Therefore, it can be said that the corrosion is accelerated by the sliding action. However, as the test advanced, as a consequence of a decrease in the contact pressure due to the larger area of contact created and the increase of COF, depassivation decreased and thus, the current had a decreasing trend [34]. When rubbing stopped, due to the anodic repassivation of the worn track surface, the current shifted cathodically to the values observed before loading.

3.3.4 Hardness Measurements

As presented in Fig. 4a, due to the work/deformation hardening of the wear track under the rubbing action of the alumina ball, the microhardness measured inside the wear track was always higher than that of the outside. Moreover, the hardness values measured in the wear track were the lowest at anodic potentiostatic polarization and the highest at cathodic potentiostatic polarization. This was due to the higher work hardening obtained under cathodic potentiostatic polarization condition as a result of the higher COF governed (see Fig. 4b). Same trend has been previously reported by Bidiville et al. on tribocorrosion of 316L austenitic stainless steel [41]. It should be noted that the decrease in the work hardening under anodic potentiostatic polarization clearly indicates the negative synergistic effect of corrosion on wear.

3.3.5 Evolution of Friction Coefficient

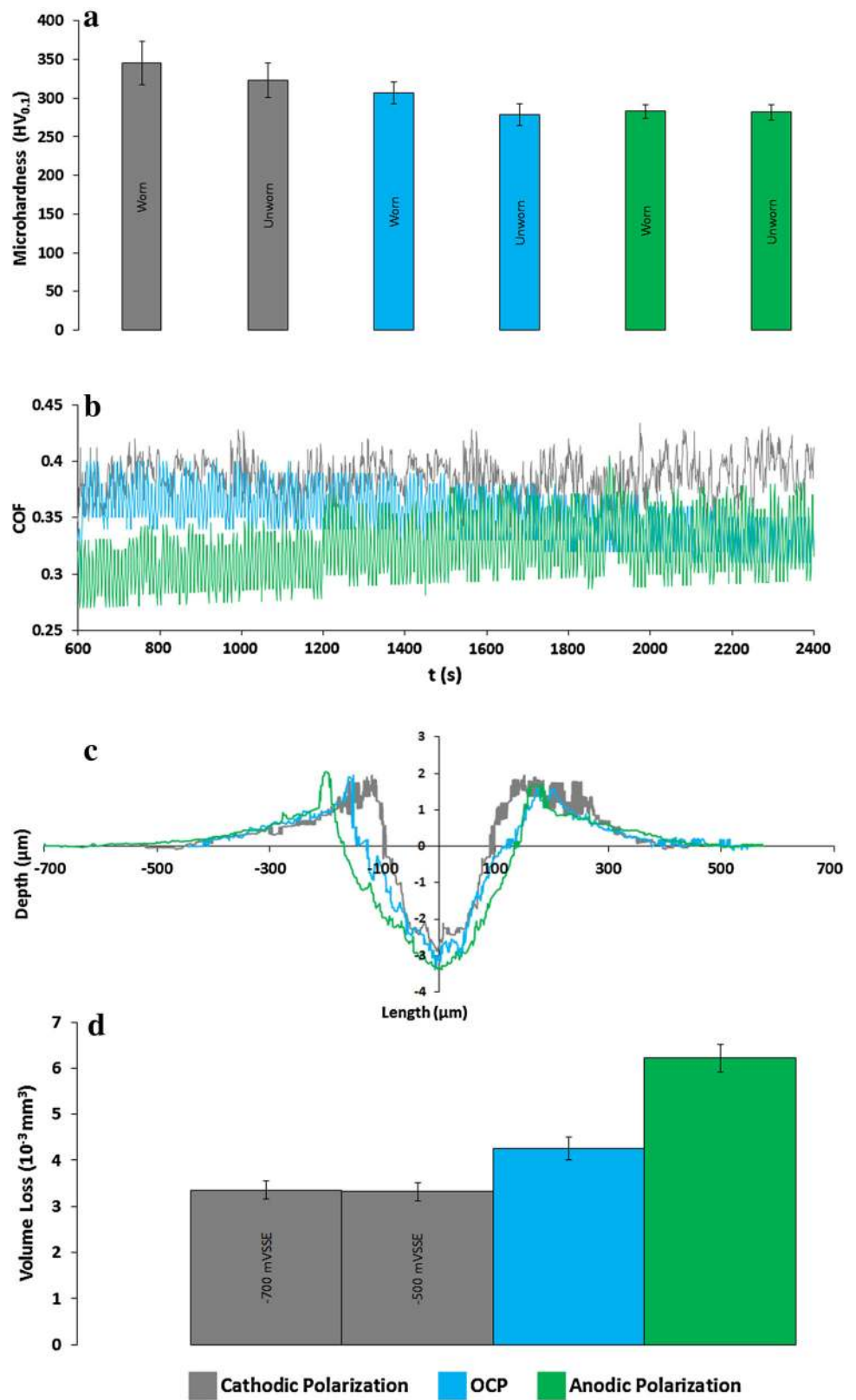
Figure 4b compares the variation of COF with time during rubbing under different testing conditions. As can be seen, COF was higher at cathodic potentiostatic polarization compared with those measured at OCP and anodic potentiostatic polarization conditions. Generally, due to the increased mechanical interlocking, rough surfaces result in higher COF. Thus, since the worn surface created under cathodic potentiostatic polarization was rougher [$(R_a)_{\text{cathodic}} = 0.86 \mu\text{m}$ vs. $(R_a)_{\text{anodic}} = 0.37 \mu\text{m}$, see also Fig. 5b], it showed higher COF.

Silva et al. [14] reported that because during tribocorrosion of UNS S32750 SDSS, the friction force is proportional to the normal load applied between the two bodies (Amontons' law), the COF is independent of the load level [42], but it depends on the applied potential. Such a potential dependency can be clearly seen in Fig. 4b and can be attributed to the benefic lubrication effect of the passive film formed on the surface of the SDSS overlay weldment under anodic potentiostatic polarization which significantly reduced the friction coefficient as well as the surface wear. Conversely, in the cathodic domain, the protective oxide film disappeared due to hydrogen evolution which cleansed the surface and made it rougher. This yielded a higher friction coefficient and thus, a lower resistance to wear.

3.3.6 Wear Topography

The worn surface topography of tribocorrosion samples was investigated by SEM and the results are compared against unworn surface in Fig. 5. At cathodic potentiostatic polarization (Fig. 5b), the wear track was free of corrosion products, but was rough including many fine abrasion marks. At OCP (Fig. 5c), the wear track was also quite

Fig. 4 **a** Microhardness values after polarization tests measured inside and outside the wear track, **b** evolution of the coefficient of friction during rubbing, **c** the surface of profiles at the middle of stroke length, and **d** total volume loss under different polarizations



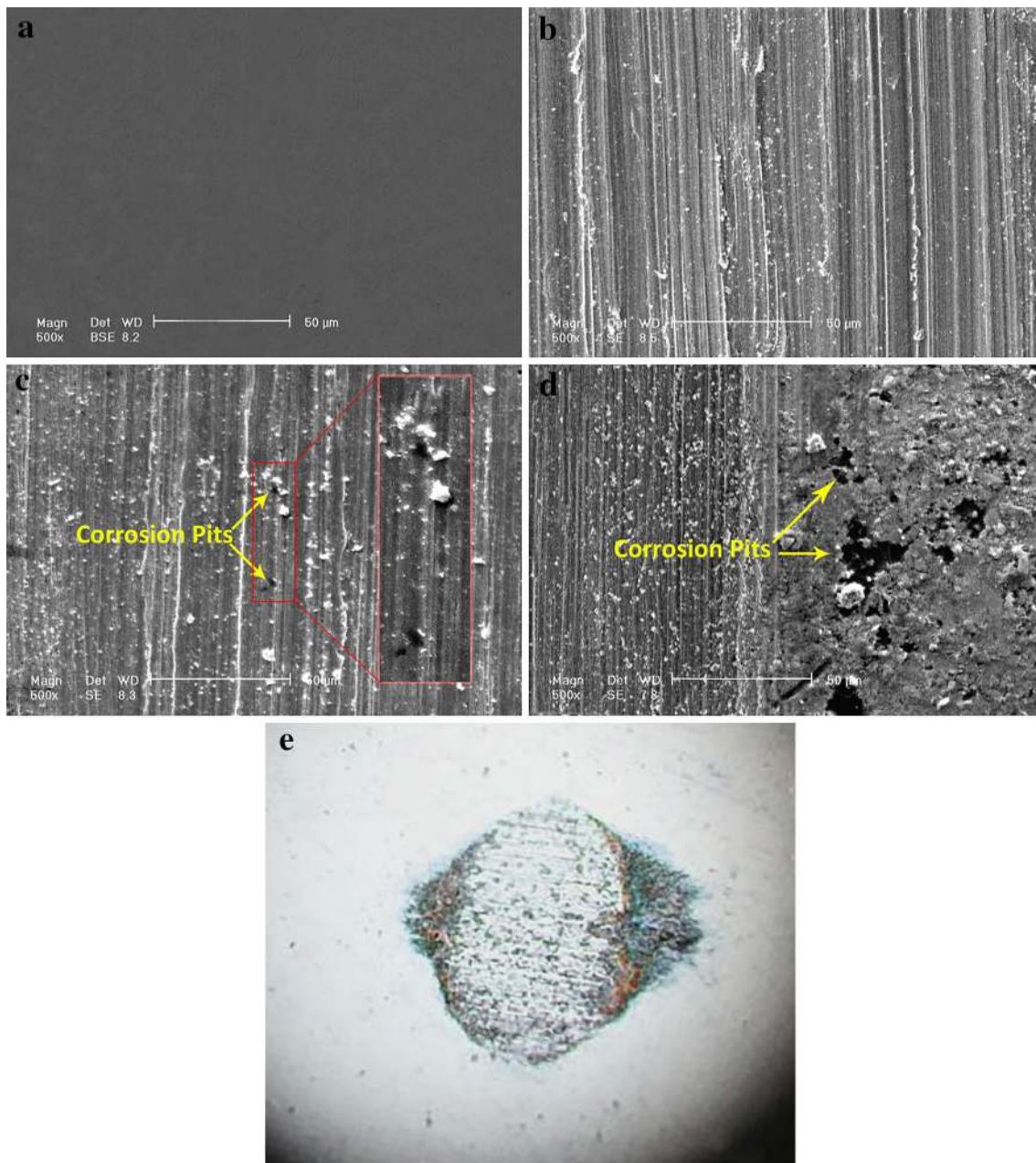


Fig. 5 a–d SEM micrograph of the **a** unworn surface ($R_a = 0.23 \mu\text{m}$) and **b–d** worn surfaces under **b** cathodic potentiostatic polarization [$(R_a)_{\text{cathodic}} = 0.86 \mu\text{m}$], **c** OCP [$(R_a)_{\text{OCP}} = 0.41 \mu\text{m}$], and

d anodic potentiostatic polarization [$(R_a)_{\text{anodic}} = 0.37 \mu\text{m}$]. **e** Optical micrograph of the alumina counterpart after anodic potentiostatic polarization

rough with many deep and wide abrasion marks, but several pits were also detectable. Based on these observations, it seems that severe abrasive wear was occurred at cathodic and OCP sliding conditions.

At anodic potential (Fig. 5d), the wear track became smoother with fine polishing marks and a few deep abrasion marks parallel to moving direction of alumina balls. Due to the production of more corrosion products that have been moved across by the alumina ball, material pile-up close to the wear track edges was more than that at OCP condition.

Since no corrosion pits were observed outside the wear track, the presence of pits at the edges of the track area indicates wear-accelerated corrosion. Generally, the mechanisms involved in tribocorrosion under anodic potentiostatic polarization are highly complex, because there are many factors affecting the surface. However, SEM micrographs of wear regions suggest that micro-polishing and occasional micro-plowing were the dominant wear mechanism.

The wear track profiles of the overlay weldment under different testing conditions are presented in Fig. 4c. In

agreement with the SEM micrographs, it can be seen that the wear tracks were extremely rough at cathodic and OCP and became smoother at anodic potential. However, this smoothness was accompanied by an increase in volume loss and thus, accumulation of wear debris at the edge of the wear track.

Observations using optical microscopy on the counter-acting alumina balls after anodic potentiostatic polarization sliding, for example, as what is demonstrated in Fig. 5e, showed insubstantial amount of metallic debris from working samples at perimeters which confirms the insignificance of third-body particles. The analysis of alumina balls showed no adhesive but inconsequential abrasive wear on the ball surface. This observation confirms the results obtained through SEM. Considering the average specific wear rate obtained [$(W_s)_{\text{ball}} = 5.37 \times 10^{-6} \text{ mm}^3/\text{Nm}$ vs. $(W_s)_{\text{specimen}} = 1.76 \times 10^{-4} \text{ mm}^3/\text{Nm}$], this result is also in agreement with the literature [40] where it is discussed that under abrasion mechanism, the degradation of alumina ball by surface is negligible.

3.3.7 Total Volume Loss Measurements

The volume losses in Fig. 4d were calculated by multiplying the cross section area obtained from roughness profiles (Fig. 4c) by wear length. According to this figure, the volume loss was higher in anodic potentiostatic polarization sliding than those at OCP and cathodic potentiostatic polarization conditions. Thus, it is obvious that the passivation enhanced the tribocorrosion degradation. This could be mainly due to two reasons: (1) wear-accelerated corrosion mainly through depassivation and (2) corrosion-accelerated wear mainly through increasing the subsurface deformation in the presence of the passive film [43]. The same result has been obtained previously in tribocorrosion testing of other passive alloys [40, 41, 44, 45].

Generally, when hydrogen embrittlement is a degradation mechanism, more hydrogen charging is expected at lower potentials and the wear volume should increase by increasing the cathodic potentiostatic polarization. However, the volume loss measured at cathodic potential of $-700 \text{ mV}_{\text{SSE}}$ was similar to that obtained at $-500 \text{ mV}_{\text{SSE}}$. This suggests that in the test solution, hydrogen embrittlement was not a key issue of concern and confirms that the material loss during cathodic potentiostatic polarization was only due to the mechanical wear.

4 Discussion

Based on the results presented in Fig. 4d, it can be concluded that cathodic protection of the overlay weldment can be effective to decrease the tribocorrosion damage,

because the wear volume measured at cathodic potentials was 22 % lower than the OCP volume loss. Moreover, since the volume loss difference at OCP and anodic potentiostatic polarization was about 46 % higher, it can be concluded that, although as reported in the literature the material removal increased with potential [46], the volume loss was not significantly affected by the applied potential, because the volume loss was increased only by 98 % when the potential was increased from cathodic to anodic as high as 1400 mV, i.e., 200 % increase. Based on these results, it is important to identify the contribution of corrosion and wear in total material removal by tribocorrosion in order to make more precise decisions for minimizing the material degradation.

4.1 Synergistic Model

Many efforts have been made by several investigators [36, 47–51] to quantify synergistic effects during tribocorrosion. In this study, to evaluate the contribution of different mechanisms involved in material degradation under anodic potentiostatic polarization, a synergistic sliding wear model was selected. In this approach, the total volume loss under static conditions (V_{tot}) is considered as the sum of wear (mechanical) volume loss (V_w), corrosion (chemical) volume loss (V_c), and the synergistic term ($V_{w \leftrightarrow c}$):

$$V_{\text{tot}} = V_w + V_c + V_{w \leftrightarrow c} \quad (2)$$

The $V_{w \leftrightarrow c}$ consists of two terms: the corrosion-accelerated wear loss ($V_{c \rightarrow w}$) and wear-accelerated corrosion loss ($V_{w \rightarrow c}$), thus

$$V_{\text{tot}} = V_w + V_c + V_{c \rightarrow w} + V_{w \rightarrow c} \quad (3)$$

$V_{w \rightarrow c}$ component can include (1) depassivation, i.e., the material loss due to the dissolution of active surfaces as a result of mechanical removal of the protective passive film and creating fresh reactive corrosion surfaces, (2) local acidification of worn surfaces which can accelerate the corrosion and prevent the formation of the passive film, (3) increased mass transport due to the turbulence of corrosive media in the contact area, (4) lowering the fatigue strength of the metal, (5) cathodically polarizing and thus, destabilizing the passive film at the surrounding unworn surfaces, and (6) locally increasing the surface roughness of the specimen and thus, enhancing the mass transfer [16].

$V_{c \rightarrow w}$, on the other hand, includes (1) removal of work-hardened surfaces by corrosion and thus, lowering the mechanical strength of material [5], (2) introduction of metallic wear particles produced by the corrosion in the form of third bodies into the wear track, (3) preferential dissolution of weaker grain boundaries by corrosive media and thus, grain loosening and eventual detachment of loose grains [52], (4) the introduction of stress concentration due

to micro-pitting, and (5) separation of plastically deformed wear debris from the metal surface by stress corrosion cracking [1]. Apart from these positive synergies, $V_{c \rightarrow w}$ can lead to antagonism by (6) blunting the crack tips by dissolution which retards the crack propagation rate [1].

As discussed, due to the absence of hydrogen embrittlement, the dissolution of metal under cathodic potential is negligible, and thus, V_w can be estimated equal to $(V_{tot})_{cathodic}$. This approximation supposes that all other conditions in the contact area, including friction coefficient, surface hardness, roughness, adhesion, etc., remained the same at all potentials, and thus, contains some natural errors.

V_{tot} in Eq. 3 can be obtained by profilometry of wear track in anodic potentiostatic polarization condition. The current measured during sliding flows mainly through the wear track [37], and thus, V_c can be calculated by applying Faraday's law [36] (Eq. 4) to the current obtained through the averaging of the current measured before sliding under anodic potentiostatic condition (I_c):

$$V_c = \frac{QMT}{nF\rho}, \quad (4)$$

where t is sliding time, $Q = \int I_c dt$, F is the Faraday's constant ($96,458 \text{ C mol}^{-1}$), ρ is the material density (7.8 g cm^{-3}), n is the valence of dissolution and oxidation, and M is the atomic mass of the alloy given by $\sum X_i M_i$, where X_i is the mole fraction and M_i is the atomic mass of the alloy constituents, i.e., Fe, Cr, Ni, and Mo. According to Eq. 4, the calculated value of V_c depends on the value of n used in the calculation. For stainless steels, both Fe and Cr dissolve with a valence of 2 in the active region. However, in the passive region, they form oxides with a valence of 3 [38]. Thus, the exact valence value is not clear for the test conditions [42]. In this study, a valence value of 3 was used to account for passive oxide film formation and dissolution at contact intervals.

It is possible to calculate $V_{w \rightarrow c}$ by applying Faraday's law to $Q_{w \rightarrow c}$. The average current during sliding under anodic potentiostatic polarization can be assumed to be wholly due to the oxide film formation and passive dissolution at contact intervals [36]. Thus, $Q_{w \rightarrow c}$ can be calculated by subtracting Q_c from the current obtained through the averaging of the current measured during sliding under anodic potentiostatic polarization ($Q_{w \leftrightarrow c}$):

$$Q_{w \rightarrow c} = Q_{w \leftrightarrow c} - Q_c \quad (5)$$

Then, $V_{c \rightarrow w}$ can be extracted from Eq. 3.

4.2 Synergistic Degradation

The contribution of different degrading components is presented in Fig. 6. It can be seen that a positive synergy

led to more volume loss and this synergy accelerated material removal 1.6 times, i.e., $V_{tot} = 1.6 (V_c + V_w)$. In other words, the synergy level was about 60 %. Moreover, it can be seen that the greatest degrading mechanisms were V_w and $V_{w \rightarrow c}$. This confirms well with the literature, because the main proposed mechanisms for degradation of passive metals in tribocorrosion are reported to be mechanical wear and depassivation, respectively [36]. Moreover, due to their relatively low surface hardness, it is generally accepted that the resistance of SDSSs to abrasion is much weaker than their corrosion resistance. Thus, great contribution of V_w in total volume loss is reasonable.

According to the above analysis, the degradation mechanism of the SDSS overlay weldment can be proposed as follows. At cathodic potentials, since no repassivation was possible, after some cycles of sliding, some bare surfaces were created. However, due to the higher COF involved, some big wear particles separated from the surface and participated in sliding. Thus, due to three-body wearing, the wear track surface was quite rough.

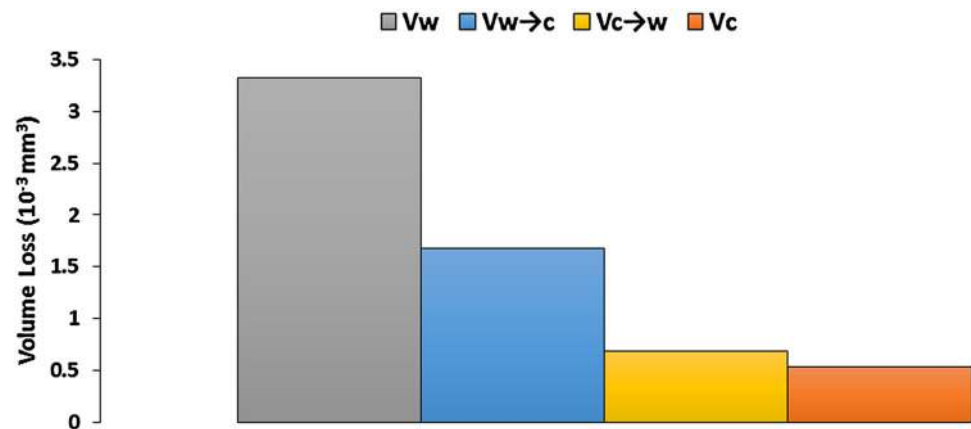
At OCP condition, the oxide film formed was not thick enough to prevent alumina slider from digging into the surface. Moreover, the corrosion loss also contributed in degradation at OCP. Thus, the removed thin oxide film regrew at each contact interval. However, compared to the cathodic potentiostatic polarization, dissolution of wear debris decreased the wear track roughness.

Clearly, at anodic potential, the oxide film formed on the surface at each contact interval became thicker than that at OCP. Thus, the repeated removal of the thicker oxide film by subsequent sliding cycles resulted in higher material loss. Several researchers [37, 43] reported a similar relationship between the thickness of the passive oxide film and the volume loss. In this condition, since wear was mainly confined to the oxide film removal, a smooth wear track surface resulted; but occasional detachment of the grains led to the formation of some scratches on the smooth surface of the track area. These detachments were mainly because of corrosion-accelerated wear as a result of the increase in the number of stress concentration defects resulting from micro-pitting (see Fig. 5).

4.2.1 Wear-Accelerated Corrosion

As discussed by Bello et al. [53], repassivation performance and passive oxide film structure are two important factors in tribocorrosion performance of stainless steels in two-body or grooving abrasion. These authors have tested three stainless steels with different passivation rates, and found that, under a constant load, the material with the best repassivation performance showed the least volume loss as a result of synergy. In the literature, there are some other reports indicating small positive [54] or even negative

Fig. 6 Dominant loss mechanisms involved in tribocorrosion



corrosion-accelerated wear synergies [53, 55] for SDSSs in NaCl-containing solutions. Moreover, Staehle [56] found that the reaction rates on the mechanically affected surface areas were one or two orders of magnitude higher than non-affected areas. Repassivation kinetics, in turn, depends on the chemical composition and microstructure of the materials. In SDSSs, the distribution of alloying elements between ferrite and austenite grains can create local chemical composition differences. However, based on the presence of well-grown GBA and WA grains, the partitioning of alloying elements on the overlay weldment's surface was appropriate, and thus, there was only 1.6 times increase in volume loss. Moreover, it should be noted that in the current study, 19.6 N load was applied, which worn both the film and bulk material simultaneously. Thus, repassivation and electrochemical resistance of overlay weldment were not the only influencing parameters. Rather, mechanical integrity also played an important role. In this regard, 60 % synergy is really negligible.

4.2.2 Corrosion-Accelerated Wear

Pitting is a well-known phenomenon for SDSSs, which is reported to take place preferentially at Cr_2N [57–60] precipitates and/or elongated γ/δ grain boundaries with sharp composition gradients [61, 62] within the microstructure. According to a previous study [26], the cooling rate from 800 to 500 °C in constant current overlay welding with exactly the same parameters was found to be about $55 \text{ }^\circ\text{C s}^{-1}$. Although such a cooling rate is not enough for precipitation of intermetallic phases, it is sufficient for formation of Cr_2N [63, 64]. As confirmed by electrochemical impedance spectroscopy [26], the presence of these nitrides resulted in a porous passive film and metastable pitting. In the presence of sliding counter body, these metastable pits can act as temporary stress risers and accelerate the wear degradation. This clearly confirms the

contribution of corrosion-accelerated wear in degradation of sample surface.

Another corrosion-accelerating wear mechanism was the decrease in the work hardening of overlay weldment under anodic potentiostatic polarization. Compared to the cathodic potentiostatic polarization, the hardness of the wear track was found to be lower under anodic tribocorrosion test. This indicates a positive synergy between corrosion and wear; as the work-hardened surfaces were removed by corrosion, the sliding wear caused more severe damage to the surface.

5 Conclusion

The present study addressed the tribocorrosion behavior of SDSS overlay weldments. The combined effect between corrosion and wear has been demonstrated by open circuit potential measurements and potentiostatic tests during tribocorrosion tests. The results of this work demonstrated that in 1 M NaCl solution, by shifting the potentiostatic potential from cathodic to anodic range, positive synergy, mainly in the form of wear-accelerated corrosion, led to accelerated material removal about 1.6 times. Under the present sliding conditions (19.6 N contact load and 1 Hz frequency), the wear particles and delaminated materials from the overlay weldment participated in wearing at cathodic potentials, causing abrasive wear and roughening of the wear track surface. However, at anodic potentials, apart from mechanical wear loss, overlay welded specimen suffered more from wear-accelerated corrosion, where material removal was dominated by repeated removal and repassivation of the metal surface during the sliding process. The principal tribocorrosion component, thus, changed from pure wear loss at cathodic potentials, to mixed wear and corrosion loss in passive potentials. Alumina counter material showed negligible reactivity against the

test materials and as a consequence, the material removal followed abrasion mechanism.

It should be pointed out that the material loss during tribocorrosion of SDSSs in the NaCl solutions is expected to depend on the contact load, applied potential, sliding time, and frequency. Silva et al. [14] showed that during the tribocorrosion measurements of SDSSs, corrosion damage takes place beyond a threshold force, and as the load level increases, the dominant wear mechanism changes. Hence, it is required that the effect of load level on the material degradation be investigated. On the other hand, Ohe et al. [2] noticed a strong dependency of the degradation mechanism of a SDSS on the passive film integrity. Thus, kinematic parameters such as sliding time and frequency can also be pivotal factors. Furthermore, the corrosion and tribocorrosion behaviors of materials in different media [6] and even in a same media with different concentrations [65] are unlike. Thus, for a complete evaluation of tribocorrosion of SDSSs, further tests need to be carried out.

Acknowledgments The authors gratefully acknowledge Masoomeh Eskandarian for her technical assistance and expert advice.

References

- Richardson TJA, Cottis BRA, Lindsay R, Lyon S, Scantlebury DJD, Stott H, Graham M (2010) Shreir's corrosion, vol 2, 1st edn. Elsevier, Manchester
- von der Ohe CB, Johnsen R, Espallargas N (2012) Multi-degradation behavior of austenitic and super duplex stainless steel - The effect of 4-point static and cyclic bending applied to a simulated seawater tribocorrosion system. *Wear* 288:39–53. doi:10.1016/j.wear.2012.02.016
- Pokhmurs'kyi V, Dovhunyk V (2010) Tribocorrosion of stainless steels (review). *Mater Sci* 46(1):87–96. doi:10.1007/s11003-010-9267-3
- Mathew MT, Srinivasa Pai P, Pourzal R, Fischer A, Wimmer MA (2009) Significance of tribocorrosion in biomedical applications: overview and current status. *Adv Tribol*. doi:10.1155/2009/250986
- Wood RJK (2007) Tribo-corrosion of coatings: a review. *J Phys D Appl Phys* 40(18):5502–5521. doi:10.1088/0022-3727/40/18/S10
- Espallargas N, Mischler S (2010) Tribocorrosion behaviour of overlay welded Ni-Cr 625 alloy in sulphuric and nitric acids: electrochemical and chemical effects. *Tribol Int* 43(7):1209–1217. doi:10.1016/j.triboint.2009.12.009
- O'Brien RL (1997) Jefferson's Welding Encyclopedia. American Welding Society, Miami
- Alves SA, Bayón R, Igartua A, Saénz de Viteri V, Rocha LA (2014) Tribocorrosion behaviour of anodic titanium oxide films produced by plasma electrolytic oxidation for dental implants. *Lubr Sci* 26(7–8):500–513. doi:10.1002/lis.1234
- Weibull I (1987) Duplex stainless steels and their application, particularly in centrifugal separators, part A: history & development. *Mater Des* 8(1):35–40. doi:10.1016/0261-3069(87)90058-6
- Gunn RN (1997) Duplex stainless steels: microstructure, properties and applications, 1st edn. Woodhead Publishing, Abington
- Weibull I (1987) Duplex stainless steels and their application, particularly in centrifugal separators, part B: corrosion resistance. *Mater Des* 8(2):82–88. doi:10.1016/0261-3069(87)90111-7
- von der Ohe CB, Johnsen R, Espallargas N (2009) Hydraulic cylinders for offshore splash zone operation: a review of piston rod failure cases and alternative concepts. In: ASME 2009 28th International Conference on Ocean, Offshore and Arctic Engineering, Honolulu, May 31–June 5, 2009. ASME, pp 1–14. doi:10.1115/OMAE2009-79039
- Takadom J (2008) Materials and surface engineering in tribology, 1st edn. Wiley-ISTE, London. doi:10.1002/9780470611524
- Silva RCC, Nogueira RP, Bastos IN (2011) Tribocorrosion of UNS S32750 in chloride medium: effect of the load level. *Electrochim Acta* 56(24):8839–8845. doi:10.1016/j.electacta.2011.07.077
- Kubecka P, Wenger F, Hyspecka L, Ponthiaux P, Galland J (1999) Tribocorrosion tests of duplex stainless steels 2205. *Acta Metall Slov* 2:93–102
- Vignal V, Mary N, Ponthiaux P, Wenger F (2006) Influence of friction on the local mechanical and electrochemical behaviour of duplex stainless steels. *Wear* 261(9):947–953. doi:10.1016/j.wear.2006.03.002
- Martin F, García C, Blanco Y, Aparicio ML (2013) Tribocorrosion behaviour of powder metallurgy duplex stainless steels sintered in nitrogen. *Tribol Int* 57:76–85. doi:10.1016/j.triboint.2012.06.032
- Von Bonin A, Hochschule A, Espallargas N, Johnson R, von der Ohe CB (2010) Evaluation of different stainless steels under tribocorrosion stress in harsh marine environment. *Junior Euromat: Corrosion, Wear, Biocompatibility*. Université de Lausanne (UNIL), Amphipôle
- Von der Ohe CB, Johnsen R, Espallargas N (2011) The Effect of Cyclic and Static Tensile Stresses on the Tribocorrosion Behavior of Austenitic and Duplex Stainless Steels in Marine Environment. Paper presented at the Corrosion, Houston, Texas, 1 Jan 2011
- Watson SW, Friedersdorf FJ, Madsen BW, Cramer SD (1995) Methods of measuring wear-corrosion synergism. *Wear* 181–183(Part 2):476–484. doi:10.1016/0043-1648(95)90161-2
- Mischler S, Ponthiaux P (2001) A round robin on combined electrochemical and friction tests on alumina/stainless steel contacts in sulphuric acid. *Wear* 248(1–2):211–225. doi:10.1016/S0043-1648(00)00559-7
- Garzón CM, Ramirez AJ (2006) Growth kinetics of secondary austenite in the welding microstructure of a UNS S32304 duplex stainless steel. *Acta Mater* 54(12):3321–3331. doi:10.1016/j.actamat.2006.03.018
- Perren RA, Suter TA, Uggowitzer PJ, Weber L, Magdowski R, Böhni H, Speidel MO (2001) Corrosion resistance of super duplex stainless steels in chloride ion containing environments: investigations by means of a new microelectrochemical method: I. Precipitation-free states. *Corros Sci* 43(4):707–726. doi:10.1016/S0010-938X(00)00087-1
- Pettersson N, Pettersson RA, Wessman S (2015) Precipitation of chromium nitrides in the super duplex stainless steel 2507. *Metall Mat Trans A* 46(3):1062–1072. doi:10.1007/s11661-014-2718-y
- Eghlimi A, Shamanian M, Raeissi K (2013) Dilution and ferrite number prediction in pulsed current cladding of super-duplex stainless steel using RSM. *J Mater Eng Perform* 22(12):3657–3664. doi:10.1007/s11665-013-0661-5
- Eghlimi A, Shamanian M, Raeissi K (2014) Effect of current type on microstructure and corrosion resistance of super duplex stainless steel claddings produced by the gas tungsten arc welding process. *Surf Coat Technol* 244:45–51. doi:10.1016/j.surfcoat.2014.01.047
- Holm R (1946) Electric contacts. Almqvist & Wiksells Boktryckeri AB, Uppsala

28. Archard JF (1953) Contact and rubbing of flat surfaces. *J Appl Phys* 24(8):981–988. doi:[10.1063/1.1721448](https://doi.org/10.1063/1.1721448)
29. Eghlimi A, Shamanian M, Eskandarian M, Zabolian A, Nezakat M, Szpunar JA (2015) Evaluation of microstructure and texture across the welded interface of super duplex stainless steel and high strength low alloy steel. *Surf Coat Technol* 264:150–162. doi:[10.1016/j.surfcoat.2014.12.060](https://doi.org/10.1016/j.surfcoat.2014.12.060)
30. Bettini E, Kivisäkk U, Leygraf C, Pan J (2014) Study of corrosion behavior of a 2507 super duplex stainless steel: influence of quenched-in and isothermal nitrides. *Int J Electrochem Sci* 9(1):61–80
31. Yang Y, Yan B, Li J, Wang J (2011) The effect of large heat input on the microstructure and corrosion behaviour of simulated heat affected zone in 2205 duplex stainless steel. *Corros Sci* 53(11):3756–3763. doi:[10.1016/j.corsci.2011.07.022](https://doi.org/10.1016/j.corsci.2011.07.022)
32. Moayed MH, Newman RC (2006) Evolution of current transients and morphology of metastable and stable pitting on stainless steel near the critical pitting temperature. *Corros Sci* 48(4):1004–1018. doi:[10.1016/j.corsci.2005.03.002](https://doi.org/10.1016/j.corsci.2005.03.002)
33. Perren RA, Suter TA, Solenthaler C, Gullo G, Uggowitz PJ, Böhni H, Speidel MO (2001) Corrosion resistance of super duplex stainless steels in chloride ion containing environments: investigations by means of a new microelectrochemical method: II. Influence of precipitates. *Corros Sci* 43(4):727–745. doi:[10.1016/S0010-938X\(00\)00088-3](https://doi.org/10.1016/S0010-938X(00)00088-3)
34. Espallargas N, Johnsen R, Torres C, Muñoz AI (2013) A new experimental technique for quantifying the galvanic coupling effects on stainless steel during tribocorrosion under equilibrium conditions. *Wear* 307(1–2):190–197. doi:[10.1016/j.wear.2013.08.026](https://doi.org/10.1016/j.wear.2013.08.026)
35. Bardal E (2004) *Corrosion and Protection*, vol 283–288. Springer, London
36. Mischler S (2008) Triboelectrochemical techniques and interpretation methods in tribocorrosion: a comparative evaluation. *Tribol Int* 41(7):573–583. doi:[10.1016/j.triboint.2007.11.003](https://doi.org/10.1016/j.triboint.2007.11.003)
37. García I, Drees D, Celis J-P (2001) Corrosion-wear of passivating materials in sliding contacts based on a concept of active wear track area. *Wear* 249(5–6):452–460. doi:[10.1016/s0043-1648\(01\)00577-4](https://doi.org/10.1016/s0043-1648(01)00577-4)
38. Sun Y, Haruman E (2011) Effect of electrochemical potential on tribocorrosion behavior of low temperature plasma carburized 316L stainless steel in 1 M H₂SO₄ solution. *Surf Coat Technol* 205(17–18):4280–4290. doi:[10.1016/j.surfcoat.2011.03.048](https://doi.org/10.1016/j.surfcoat.2011.03.048)
39. Martin É, Azzi M, Salishchev GA, Szpunar J (2010) Influence of microstructure and texture on the corrosion and tribocorrosion behavior of Ti-6Al-4 V. *Tribol Int* 43(5–6):918–924. doi:[10.1016/j.triboint.2009.12.055](https://doi.org/10.1016/j.triboint.2009.12.055)
40. Chen J, Yan FY, Chen BB, Wang JZ (2013) Assessing the tribocorrosion performance of Ti-6Al-4V, 316 stainless steel and Monel K500 alloys in artificial seawater. *Mater Corros* 64(5):394–401. doi:[10.1002/maco.201106249](https://doi.org/10.1002/maco.201106249)
41. Bidiville A, Favero M, Stadelmann P, Mischler S (2007) Effect of surface chemistry on the mechanical response of metals in sliding tribocorrosion systems. *Wear* 263(1–6):207–217. doi:[10.1016/j.wear.2007.01.066](https://doi.org/10.1016/j.wear.2007.01.066)
42. Al-Bender F, De Moerlooze K (2010) On the relationship between normal load and friction force in pre-sliding frictional contacts. Part 1: theoretical analysis. *Wear* 269(3–4):174–182. doi:[10.1016/j.wear.2010.02.010](https://doi.org/10.1016/j.wear.2010.02.010)
43. Guadalupe Maldonado S, Mischler S, Cantoni M, Chitty W-J, Falcand C, Hertz D (2013) Mechanical and chemical mechanisms in the tribocorrosion of a Stellite type alloy. *Wear* 308(1–2):213–221. doi:[10.1016/j.wear.2013.04.007](https://doi.org/10.1016/j.wear.2013.04.007)
44. Mischler S, Spiegel A, Landolt D (1999) The role of passive oxide films on the degradation of steel in tribocorrosion systems. *Wear* 225–229(Part 2 (0)):1078–1087. doi:[10.1016/s0043-1648\(99\)00056-3](https://doi.org/10.1016/s0043-1648(99)00056-3) **Part 2 (0):1078-1087**
45. Muñoz AI, Julián LC (2010) Influence of electrochemical potential on the tribocorrosion behaviour of high carbon CoCrMo biomedical alloy in simulated body fluids by electrochemical impedance spectroscopy. *Electrochim Acta* 55(19):5428–5439. doi:[10.1016/j.electacta.2010.04.093](https://doi.org/10.1016/j.electacta.2010.04.093)
46. Takadom J (1998) The triboelectrochemical cell: a new apparatus for tribocorrosion studies. *Tribotest* 4(4):437–440. doi:[10.1002/tt.3020040409](https://doi.org/10.1002/tt.3020040409)
47. Jemmely P, Mischler S, Landolt D (2000) Electrochemical modeling of passivation phenomena in tribocorrosion. *Wear* 237(1):63–76. doi:[10.1016/s0043-1648\(99\)00314-2](https://doi.org/10.1016/s0043-1648(99)00314-2)
48. Diomidis N, Celis J-P, Ponthiaux P, Wenger F (2009) A methodology for the assessment of the tribocorrosion of passivating metallic materials. *Lubr Sci* 21(2):53–67. doi:[10.1002/lis.73](https://doi.org/10.1002/lis.73)
49. Diomidis N, Celis J-P, Ponthiaux P, Wenger F (2010) Tribocorrosion of stainless steel in sulfuric acid: identification of corrosion-wear components and effect of contact area. *Wear* 269(1–2):93–103. doi:[10.1016/j.wear.2010.03.010](https://doi.org/10.1016/j.wear.2010.03.010)
50. Papageorgiou N, von Bonin A, Espallargas N (2014) Tribocorrosion mechanisms of NiCrMo-625 alloy: an electrochemical modeling approach. *Tribol Int* 73:177–186. doi:[10.1016/j.triboint.2014.01.018](https://doi.org/10.1016/j.triboint.2014.01.018)
51. Jiang J, Stack MM, Neville A (2002) Modelling the tribo-corrosion interaction in aqueous sliding conditions. *Tribol Int* 35(10):669–679. doi:[10.1016/S0301-679X\(02\)00058-0](https://doi.org/10.1016/S0301-679X(02)00058-0)
52. Arenas MA, Conde A, de Damborenea JJ (2013) The role of mechanically activated area on tribocorrosion of CoCrMo. *Metall Mat Trans A* 44(9):4382–4390. doi:[10.1007/s11661-013-1759-y](https://doi.org/10.1007/s11661-013-1759-y)
53. Bello JO, Wood RJK, Wharton JA (2007) Synergistic effects of micro-abrasion–corrosion of UNS S30403, S31603 and S32760 stainless steels. *Wear* 263(1–6):149–159. doi:[10.1016/j.wear.2006.12.044](https://doi.org/10.1016/j.wear.2006.12.044)
54. Neville A, Hu X (2001) Mechanical and electrochemical interactions during liquid–solid impingement on high-alloy stainless steels. *Wear* 251(1–12):1284–1294. doi:[10.1016/S0043-1648\(01\)00757-8](https://doi.org/10.1016/S0043-1648(01)00757-8)
55. Wood RJK (1992) Effets combinés de l'érosion et de la corrosion pour les matériaux des conduites d'écoulements polyphasiques (Erosion-corrosion synergism for multi-phase flowline materials). *La Houille Blanche* 7–8:605–610. doi:[10.1051/lhb/1992065](https://doi.org/10.1051/lhb/1992065)
56. Staehle RW (2007) Transient stability of passive films in aqueous solutions. *Corros Sci* 49(1):7–19. doi:[10.1016/j.corsci.2006.05.006](https://doi.org/10.1016/j.corsci.2006.05.006)
57. Zhang L, Jiang Y, Deng B, Zhang W, Xu J, Li J (2009) Effect of aging on the corrosion resistance of 2101 lean duplex stainless steel. *Mater Charact* 60(12):1522–1528. doi:[10.1016/j.matchar.2009.08.009](https://doi.org/10.1016/j.matchar.2009.08.009)
58. Chan K, Tjong S (2014) Effect of secondary phase precipitation on the corrosion behavior of duplex stainless steels. *Materials* 7(7):5268–5304. doi:[10.3390/ma7075268](https://doi.org/10.3390/ma7075268)
59. Kim J-S, Kim S-T, Lee I-S, Jang S-H, Park Y-S, Kim K-T, Kim Y-S (2012) Mechanism of localized corrosion and phase transformation of tube-to-tube sheet welds of hyper duplex stainless steel in acidified chloride environments. *Mater Trans* 53(12):2166–2174. doi:[10.2320/matertrans.M2012243](https://doi.org/10.2320/matertrans.M2012243)
60. Jang S-H, Kim S-T, Lee I-S, Park Y-S (2011) Effect of shielding gas composition on phase transformation and mechanism of pitting corrosion of hyper duplex stainless steel welds. *Mater Trans* 52(6):1228–1236. doi:[10.2320/matertrans.M2010414](https://doi.org/10.2320/matertrans.M2010414)
61. Ferro P, Tiziani A, Bonollo F (2008) Influence of induction and furnace postweld heat treatment on corrosion properties of SAF 2205 (UNS 31803). *Weld J* 87(12):298s–306s
62. Batista SRF, Kuri SE (2004) Aspects of selective and pitting corrosion in cast duplex stainless steels. *Anti-Corros Methods Mater* 51(3):205–208. doi:[10.1108/00035590410533156](https://doi.org/10.1108/00035590410533156)
63. Ramirez AJ, Brandi SD, Lippold JC (2004) Secondary austenite and chromium nitride precipitation in simulated heat affected

- zones of duplex stainless steels. *Sci Technol Weld Joining* 9(4):301–313. doi:[10.1179/136217104225021715](https://doi.org/10.1179/136217104225021715)
64. Wang H-S (2005) Effect of welding variables on cooling rate and pitting corrosion resistance in super duplex stainless weldments. *Mater Trans* 46(3):593–601. doi:[10.2320/matertrans.46.593](https://doi.org/10.2320/matertrans.46.593)
65. Mischler S, Rosset E, Stachowiak GW, Landolt D (1993) Effect of sulphuric acid concentration on the rate of tribocorrosion of iron. *Wear* 167(2):101–108. doi:[10.1016/0043-1648\(93\)90314-C](https://doi.org/10.1016/0043-1648(93)90314-C)